Mechanically robust and thermodynamically stable FeSc₂Z₄ (Z = S, Se) spinels for future spintronic architectures

Ateeq Anwar,[a] N. A. Noor,*[a] Ghulam M. Mustafa, [ID] *[b] Shahid Atiq, [ID] [c] A. Ibrahim[d] and A. Laref [ID] [e]

Spintronics, an emerging paradigm in next-generation electronics, fundamentally relies on materials that exhibit spin polarization, often achieved through intrinsic magnetic ordering in semiconductors as well as in metals. In this paper, the structural, mechanical, electronic, and thermodynamic characteristics of FeSc₂Z₄ (Z = S, Se) spinel compounds are systematically investigated using the density functional theory-based WIEN2k code. The calculated lattice constants are found to be 10.35 Å for FeSc₂S₄ and 10.83 Å for FeSc₂Se₄, comparable to the experimental lattice constants. Negative formation enthalpies of −1.67 eV (FeSc₂S₄) and −1.13 eV (FeSc₂Se₄) confirm that FeSc₂S₄ exhibits comparatively higher thermodynamic stability. Additionally, positive values of phonon frequency indicate both spinels are structurally stable. Elastic properties reveal mechanical robustness and ductility, as reflected by Poisson ratios of 0.31 and 0.32, and B_0/G ratios of 2.31 and 2.44, respectively. However, electronic properties reveal that with increasing pressure from 0 to 4 GPa, both FeSc₂S₄ and FeSc₂Se₄ exhibit a monotonic reduction in their direct band gaps, with FeSc₂S₄ undergoing a transition to a half-metallic ferromagnetic state at higher pressures. Magnetic analysis yields a total magnetic moment of $4.00\mu_B$ per formula unit in both materials, primarily originating from the Fe-site, indicating ferrimagnetic behavior. Furthermore, the values of entropy and Debye temperature using the quasi-harmonic Debye model-based GIBBS2 framework reflect the phonon softening, lattice stiffening, and anharmonic effects. These thermodynamic insights further support the thermal stability and vibrational integrity of FeSc₂Z₄ (Z = S, Se) spinels, underscoring their potential for spintronic and magneto-electronic device applications.

1. Introduction

The escalating demand for faster, energy-efficient, and miniaturized electronic devices has outpaced the capabilities of traditional charge-based electronics, prompting the exploration of alternative paradigms for information processing and storage.[1] Spintronics has emerged as a transformative technology that leverages the intrinsic spin of the electron, alongside its charge, to enable multifunctional device operations with reduced power consumption and enhanced performance.[2] By exploiting spin degrees of freedom, spintronic devices promise non-volatility, higher data processing speeds, and

seamless integration with existing CMOS architectures, thereby addressing key limitations in conventional semiconductor technologies.[3] The advent of magnetic tunnel junctions, spin-transfer torque mechanisms, and spin–orbit torque switching has already revolutionized applications such as magnetic random-access memory (MRAM) and logic in memory devices.[4] Moreover, the integration of spintronic materials with emerging platforms, including two-dimensional systems, topological insulators, and multiferroics, has unlocked novel quantum phenomena, enabling reconfigurable architectures for neuromorphic computing and quantum information technologies.[5,6] In the context of next-generation electronics, where sustainability, speed, and functionality converge as core imperatives, spintronics holds profound potential to reshape device design and system-level architectures.[7] Thus, understanding and harnessing spin-dependent phenomena at the nano-scale is central to the development of scalable, low-energy, and intelligent electronic systems for future information and energy technologies.[8]

Among the diverse classes of materials investigated for spintronic applications, half-metallic compounds have garnered particular attention due to their unique electronic

[a]Department of Physics, University of Sargodha, 40100 Sargodha, Pakistan. E-mail: naveed.noor@uos.edu.pk

[b]Department of Physics, Division of Science and Technology, University of Education, Lahore, Punjab 54770, Pakistan. E-mail: gmmustafa1025@gmail.com

[c]Center of Excellence in Solid State Physics, University of the Punjab, Lahore, Pakistan

[d]Department of Physics, College of Science, King Khalid University, P. O. Box: 9004, 61413, Abha, Asir, Kingdom of Saudi Arabia

[e]Department of Physics and Astronomy, College of Science, King Saud University, Riyadh, 11451, Kingdom of Saudi Arabia

structure exhibiting metallic response for one spin configuration and insulating or semiconducting character for the opposite. This results in 100% spin-polarization at the Fermi-level, a critical requirement for achieving highly efficient spin injection and detection in spintronic devices. Half-metallic ferromagnets, such as Heusler alloys, manganites, spinel chalcogenides, and certain transition metal oxides, offer tunable magnetic and transport properties, thermal stability, and compatibility with conventional fabrication processes.[9,10] Building upon the foundational role of half-metallic materials in enabling spin-polarized transport, transition-metal spinels have emerged as a pivotal class for next-generation spintronic technologies. These compounds, typically with the general formula AB_2X_4 (X = O, S, Se), exhibit tunable ferrimagnetism and electronic structures conducive to achieving half-metallicity.[11] Spinel chalcogenides, in particular, exhibit higher electrical conductivity and reduced carrier scattering, making them excellent candidates for low-resistance spin injection and detection.[12,13] Notably, spinel chalcogenides exhibit pronounced pressure sensitivity due to their more compressible lattices and covalent bonding characteristics, making them ideal candidates for tunable spintronic architectures.[14,15]

Özdemir and Balmumcu (2024) conducted electronic and mechanical property calculations of VCo_2O_4 using the same computational approach employed by Ak *et al.*,[16] which confirmed its half-metallic ferromagnetism with $10.00\mu_B$ f.u.$^{-1}$ magnetic moment, an equilibrium lattice constant of 8.34 Å, and increasing band gaps from 1.262 eV (GGA) to 1.286 eV (GGA + 4 eV); in addition, the material exhibited mechanical stability, ductility, and a Debye temperature of 565 K.[17,18] Extending the scope, Özdemir *et al.* (2024) investigated the VRu_2Br_4 spinel using a methodology similar to that employed in their previous study, where FM phase was found to be stable, with lattice parameter about 10.93 Å, magnetic moment of $10.00\mu_B$ f.u.$^{-1}$ and tunable band-gaps from 0.210 (GGA) to 1.718 eV (GGA + 3 eV); notably, material exhibited ductile behavior at 0 GPa (B/G = 2.48, ν = 0.322) which shifted to brittleness under 10 GPa pressure, and showed a Debye temperature of 257.22 K.[19,20] Raza *et al.* (2025) investigated $MnSc_2X_4$ (X = S, Se) spinels and found them to possess direct band gaps, static dielectric constants of 6.5 and 8.5, and high Seebeck coefficients (242–251 $\mu V\ K^{-1}$). The materials further demonstrated ferromagnetism with a high local magnetic moment and exhibited both thermodynamic and mechanical stability, thereby making them promising for optoelectronic and thermoelectric devices.[21–24] In a complementary investigation, Jamaï *et al.* (2024) evaluated XIn_2M_4 (X = Cd, Zn; M = S, Se, Te) spinels and reported indirect band gaps ranging from 2.294 eV ($CdIn_2S_4$) to 0.219 eV ($ZnIn_2Te_4$), along with strong UV-visible absorption and excellent structural stability. The figure of merit values between 0.725–0.803 at 300 K further supported their appropriateness for thermoelectric devices.[25]

The primary purpose of the current study is to comprehensively examine the structural, mechanical, electronic, magnetic, and thermodynamic characteristics of $FeSc_2Z_4$ (Z = S, Se) spinels under varying pressures using first-principles calculations. Specifically, we explore their structural stability, elastic anisotropy, electronic band-gap modulation under pressure, magnetic ordering, and thermodynamic response using the quasi-harmonic Debye model. This holistic approach not only establishes the suitability of these compounds for spintronic and magneto-electronic devices but also provides insights into their pressure-dependent multifunctionality, which has remained largely unexplored in prior studies.

2. Computational methodology

In this study, spin-polarized density functional theory (DFT) was utilized to explore structural, electronic, magnetic, and thermodynamic response of spinel-type chalcogenides $FeSc_2Z_4$ (Z = S, Se). All simulations were conducted utilizing the full-potential linearized augmented plane wave plus local orbital (FP-LAPW + lo) approach, as executed in the WIEN2k computational code,[26,27] which offers high accuracy for complex transition metal compounds due to its all-electron nature and flexible treatment of potential within atomic spheres and interstitial regions. To accurately capture the ground-state structural parameters, we employed the Perdew–Burke–Ernzerhof revised for solids (PBEsol) function within the generalized gradient approximation (GGA), owing to its improved performance in predicting equilibrium geometries and cohesive energies for crystalline solids. For detailed electronic structure analysis, particularly to address the well-known underestimation of band gaps within conventional GGA, we utilized Tran–Tran–Blaha modified Becke–Johnson (TB-mBJ) exchange potential.[28] The PBEsol functional was employed for structural optimization and mechanical property calculations because it is specifically designed to improve the description of equilibrium properties of densely packed solids and generally provides more accurate lattice constants compared to standard GGA. In contrast, the Tran–Blaha modified Becke–Johnson (TB-mBJ) potential was used for electronic structure calculations, as it is widely recognized for yielding significantly improved band gap estimations for semiconductors and correlated materials compared to conventional GGA or LDA approaches. The combined use of PBEsol and TB-mBJ thus ensures reliable structural stability analysis alongside more realistic electronic property predictions for $FeSc_2Z_4$ (Z = S, Se) spinels.

Numerical convergence was ensured through careful selection of computational parameters. The product of the smallest muffin tin radius (R_{MT}) and plane wave cut-off (K_{max}) was fix at $R_{MT}K_{max} = 8$, consistent with convergence criteria established for systems containing heavy elements and transition metals. The muffin-tin radii were chosen as: 1.90, 1.70, 1.85, and 2.10 a.u. for Fe, Sc, S, and Se, respectively. These values were optimized to avoid overlap between adjacent spheres while ensuring sufficient basis function flexibility inside the atomic spheres. An energy cutoff of −6 Ry was applied to separate core and valence states, ensuring stable and accurate treatment of semi-core states. Additionally, the maximum angular momentum quantum number $l_{max} = 10$ was selected for partial wave expansion inside the muffin-tins, which is adequate for capturing the d- and f-electron character of transition metals. The charge density's Fourier expansion was truncated at $G_{max} =$

18 Ry, providing a balanced trade-off between computational efficiency and accuracy. The Brillouin zone was sampled utilizing a dense Monkhorst–Pack grid comprising 1000 k-points, which was determined to yield converged total energy values. Beyond this k-point density, the total energy variation was found to be negligible, indicating convergence with respect to reciprocal space sampling. In addition, the thermodynamic properties of $FeSc_2Z_4$ (Z = S, Se) were evaluated utilizing the quasi-harmonic Debye model as applied in the Gibbs2 program interfaced with WIEN2k. This model enables computation of key thermodynamic parameters against temperature and pressure.[29]

3. Results and discussion

3.1. Structural analysis

Fig. 1 demonstrates the crystallographic structure of cubic spinel $FeSc_2Z_4$ (Z = S, Se) compounds, depicted in both ball-and-stick and polyhedral representations. In this spinel framework, Fe atoms (blue) occupy tetrahedral (A) sites, while Sc atoms (pink) are located at the octahedral (B) sites, coordinated by S or Se anions (yellow) to form a face-centered cubic lattice. These compounds crystallize in the well-known $Fd\bar{3}m$ (#227) space group.[30] To determine the magnetic ground state, total energy computations were performed for both ferromagnetic (FM) and antiferromagnetic (AFM) configurations using spin-polarized DFT. The total energy was computed against unit cell volume, and energy–volume (E–V) curves are presented in Fig. 2(a) and (b) for $FeSc_2S_4$ and $FeSc_2Se_4$, respectively. A clear energetic preference for the FM configuration was observed, as the FM state consistently exhibits lower total energy relative to the AFM counterpart. This energy difference confirms the greater thermodynamic stability of the FM phase. Furthermore, to analyze the thermodynamic stability of these spinels, the enthalpy of formation (ΔH_f) was computed using the following expression:[31]

$$\Delta H_f = E_{total}(Fe_lSc_mZ_n) - lE_{Fe} - mE_{Sc} - nE_Z \quad (1)$$

Here, E_{Total} represents total ground-state energy per formula unit of spinel structure, and E_{Fe}, E_{Sc}, and E_Z denote the respective ground-state energies of the elemental constituents in their stable forms. The coefficients l, m, and n represent the number of Fe, Sc, and S/Se atoms per formula unit.

The computed values of formation energy, as tabulated in Table 1, are negative for both spinel compounds, indicating that the materials are thermodynamically stable relative to their constituent elements. Notably, ΔH_f is less negative for $FeSc_2Se_4$ than for $FeSc_2S_4$, suggesting a slight reduction in stability upon substituting S with the larger Se anion. This trend is consistent with the weaker Sc–Se bonding due to increased bond length, arising from the larger ionic radius of Se^{2-} compared to S^{2-}. To extract the fundamental structural parameters at equilibrium, including the lattice constant a_0 and bulk modulus B_0, volume optimization was performed in the FM state. The equation of state proposed by Murnaghan, in conjunction with the PBEsol-GGA functional, was employed to fit the E–V data and determine the equilibrium volume. As expected, an increase in the lattice constant from $FeSc_2S_4$ and $FeSc_2Se_4$ was observed, attributed to the substitution of S by the larger Se anion, which increases the average interatomic distance. Same trend of lattice constant were also absorbed in other theoretical reported work for spinels $MnSc_2S_4$ and $MnSc_2Se_4$.[32] Correspondingly, a decrease in bulk modulus is noted, reflecting the more compressible nature of the Se-based compound. This inverse relationship between lattice parameter and bulk modulus is consistent with fundamental principles of solid-state physics, where larger unit cell volumes generally correlate with softer mechanical behavior due to weaker interatomic bonding. In Table 1, calculated value of lattice constant for $FeSc_2S_4$ is comparable to experimental values.[33]

3.2. Mechanical properties

The mechanical behavior of $FeSc_2S_4$ and $FeSc_2Se_4$ spinel compounds was systematically investigated by evaluating their independent second-order elastic constants as C_{11}, C_{12}, and C_{44}. These constants are fundamental for describing the elastic
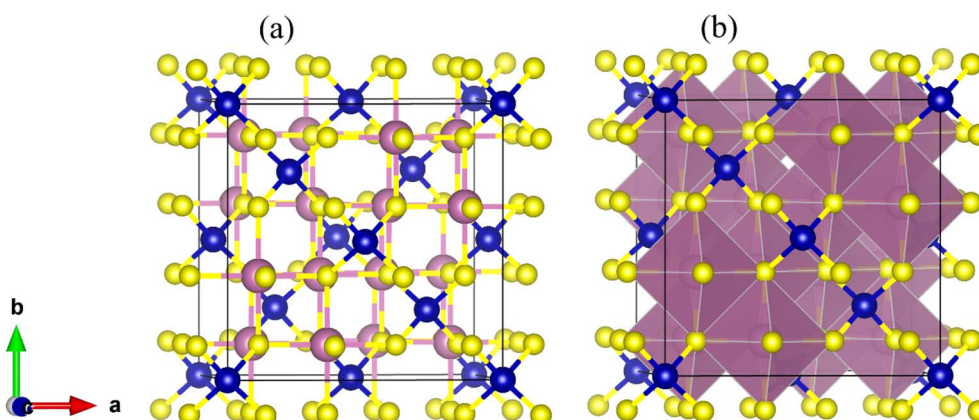

Fig. 1 Unit cell of $FeSc_2Z_4$ (Z = S, Se) (a) ball-stick format and (b) polyhedral format. The Fe, Sc and S/Se ions are represented by purple, pink and yellow color balls.
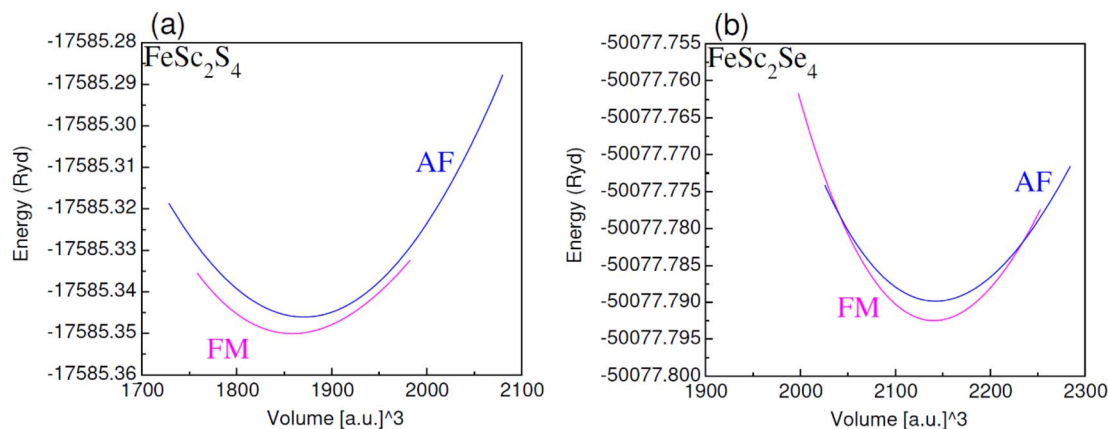
Fig. 2 The volume optimization plots of spinels (a) $FeSc_2S_4$, (b) $FeSc_2Se_4$ in FM and AFM spin-orientations.

response of cubic crystals and serve as the basis for determining key mechanical moduli.[34] The calculated elastic constants were found to satisfy the Born mechanical stability condition for cubic systems, namely $C_{11} > 0$, $C_{11} - C_{12} > 0$, and $C_{11} + 2C_{12} > 0$, thereby confirming the mechanical stability of both compositions under ambient conditions. Using the obtained elastic constants, the bulk (B), shear (G), and Young's (E) moduli were obtained from standard Voigt–Reuss–Hill averaging schemes. The calculated values are summarized in Table 1. Notably, the bulk modulus values derived from elastic constants show excellent agreement with those obtained from structural optimization, validating the mechanical robustness of these spinel structures. Such agreement further indicates the intrinsic resistance of these materials to volumetric compression. To assess the brittle or ductile character of the investigated spinels, Pugh ratio (B/G) and Poisson (ν) ratios were evaluated. According to established criteria, a B/G value exceeding 1.75 and a Poisson's ratio > 0.26 are indicative of ductile behavior. The calculated values of B/G are 2.31 for $FeSc_2S_4$ and 2.44 for $FeSc_2Se_4$, while the corresponding Poisson's ratios are 0.31 and 0.32, respectively.[35] These results consistently suggest a ductile mechanical response in both compounds, which is a favorable attribute for applications requiring mechanical resilience, such as thermo-mechanical energy devices and robust electronic platforms. The calculated B/G ratios and Poisson's ratios for $FeSc_2S_4$ and $FeSc_2Se_4$ are well above the critical values, confirming their ductile nature. Such ductility is advantageous for applications requiring resistance to fracture and mechanical resilience under operational stress. Similar trends of

mechanical robustness have also been reported in recently synthesized MAX-phase compounds and solid solutions, where a strong correlation between elastic constants and ductility indicators was established.[36,37] These comparisons validate that the mechanical behavior of $FeSc_2Z_4$ (Z = S, Se) spinels is consistent with other ductile and thermodynamically stable systems, thereby highlighting their suitability for spintronic and device-oriented applications.

Elastic anisotropy is an intrinsic and critical characteristic of crystalline materials, directly influencing their mechanical stability, deformation behavior, and phonon transport properties.[38] Anisotropy arises from the direction-dependent variation in mechanical response, whereby physical quantities such as elastic moduli vary with crystallographic orientation. In contrast, isotropic materials exhibit uniform mechanical behavior regardless of direction, maintaining constant elastic responses across all axes. To assess the elastic anisotropy of $FeSc_2Z_4$ (Z = S, Se), three-dimensional surface representations of linear compressibility (β), Young (Y), shear (G) moduli, and Poisson ratio (ν) were constructed and are illustrated in Fig. 3. In an ideal isotropic solid, these surfaces assume a perfect spherical geometry, whereas any deviation from sphericity provides a direct visual and quantitative indication of anisotropic behavior. The pronounced deformation from spherical symmetry observed in $FeSc_2S_4$, particularly in the β and G surfaces, underscores its substantial elastic anisotropy. Quantitative insights are provided by calculating the 98 maximum and minimum values for each elastic parameter, along with their corresponding ratios (β_{max}/β_{min}, Y_{max}/Y_{min}, G_{max}/G_{min}, and

Table 1 The ground state lattice constants a_0 (Å), bulk modulus B_0 (GPa), enthalpy of formation ΔH_f (eV), and elastic parameters, calculated for $FeSc_2S/Se_4$

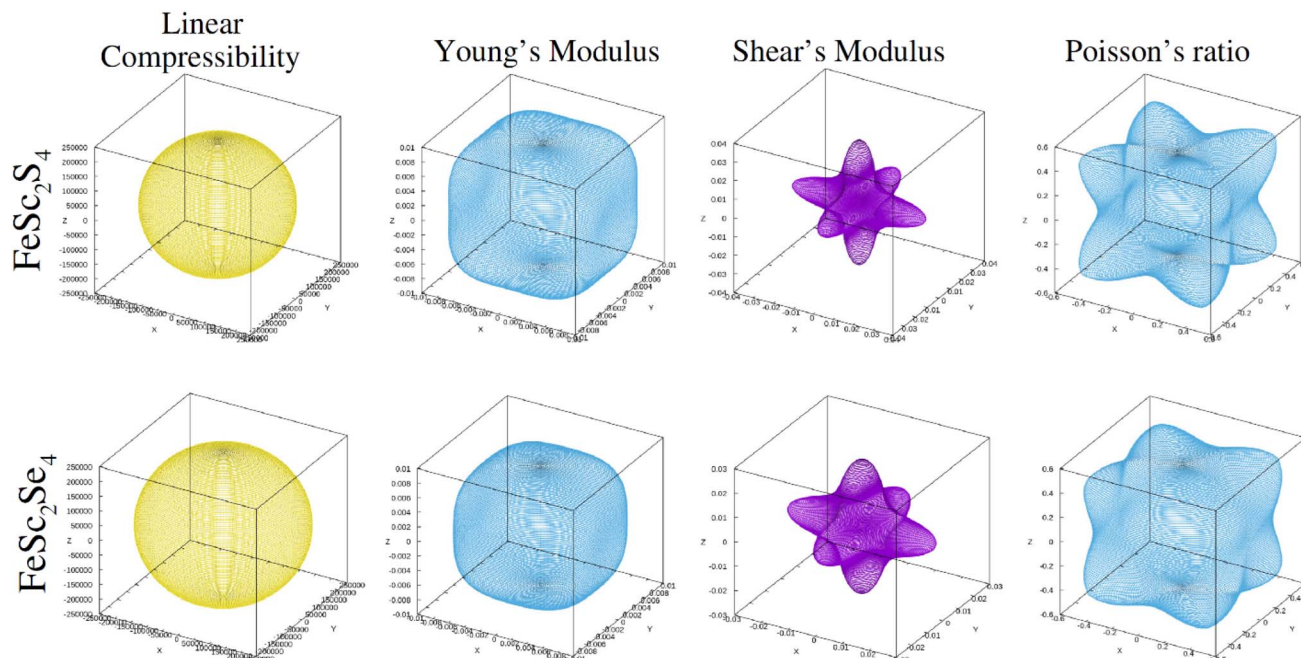| Composition	a_0 (Å)	B_0 (GPa)	ΔH_f (eV)	C_{11}	C_{12}	C_{44}	B_0	G	Y	ν	B_0/G
$FeSc_2S_4$	10.35	74.33	−1.67	118.73	50.37	30.03	73.15	31.62	82.92	0.31	2.31
Exp.	10.51[a]										
$FeSc_2Se_4$	10.83	82.90	−1.13	121.74	62.08	36.80	82.80	33.71	88.99	0.32	2.44

[a] Ref. 33.

Fig. 3 3-D representation of linear compressibility (β), Young's modulus (Y), shear modulus (G) and Poisson's ratio (v) for FeSc$_2$Z$_4$ (Z = S, Se).

v_{max}/v_{min}), as cited in Table 2. In isotropic media, these ratios approach unity, whereas deviations signal the extent of anisotropy. For FeSc$_2$S$_4$, the computed ratios were: $\beta_{max}/\beta_{min} = 1.00$, $Y_{max}/Y_{min} = 1.54$, $G_{max}/G_{min} = 5.48$, and $v_{max}/v_{min} = 0.42$. These values clearly indicate that FeSc$_2$S$_4$ exhibits significant anisotropy in both shear and Young's moduli, with particularly high anisotropy in shear response. In contrast, FeSc$_2$Se$_4$ show relatively lower anisotropic ratios, implying a more uniform elastic behavior. The pronounced elastic anisotropy observed in FeSc$_2$S$_4$ can be attributed to the stronger directional bonding characteristics associated with Fe–S and Sc–S interactions, which impart significant variation in mechanical stiffness and resistance to deformation along different crystallographic axes.[39] In contrast, the substitution of sulfur with the larger and more polarizable selenium anion in FeSc$_2$Se$_4$ introduces increased lattice softness and enhanced flexibility, which act to homogenize the mechanical response across directions and thereby reduce the extent of elastic anisotropy. This reduction in anisotropy from FeSc$_2$S$_4$ to FeSc$_2$Se$_4$ underscores a well-defined structure–property relationship, wherein chalcogen substitution influences not only the equilibrium lattice constants and bonding geometry but also directional dependence of elastic properties.[40] So, such anisotropic behavior plays

a pivotal role in analyzing mechanical stability and functional applicability of these compounds, particularly in fields where stress-induced mechanical response and directional mechanical integrity are critical, such as in magnetostriction, spintronic, and pressure-tunable optoelectronic applications.

3.3. Electronic structure analysis for FeSc$_2$S$_4$

The electronic configuration of a material fundamentally influences its intrinsic properties and determines its suitability for various electronic applications. Among these properties, the energy band-gap serves as a pivotal parameter for devices such as memory units, smart electronics, and spintronic systems, as it directly affects both their operational efficiency and performance capabilities. This band-gap plays a crucial role in modulating charge transportation and spin within electronic architectures, thereby enabling essential functionalities like data storage, signal processing, and spin manipulation. To obtain a precise estimation of the electronic characteristics of the FeSc$_2$Z$_4$ (Z = S, Se) compounds, the TB-mBJ potential was employed as depicted in Fig. 4 and 5. At 0 GPa (Fig. 4(a)), the band edges of FeSc$_2$S$_4$ lie at the same (Γ) symmetry point, exhibiting a direct band-gap semiconducting nature in the spin

Table 2 Anisotropy (A) in the elastic moduli and Poisson's ratios of FeSc$_2$X$_4$ (X = S, Se)

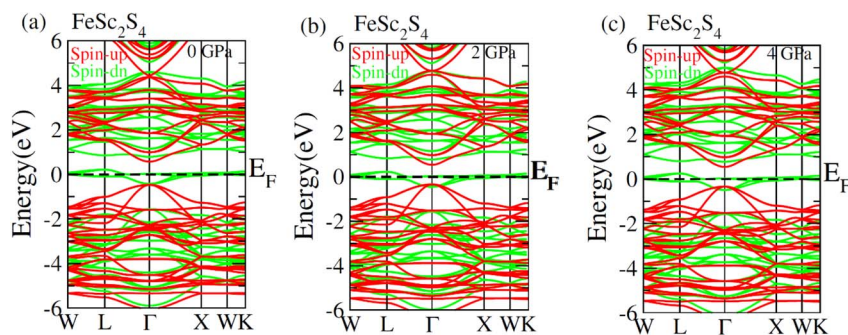| Parameters	Linear compressibility (β) (TPa^{-1})			Young's modulus (Y) (GPa)			Shear modulus (G) (GPa)			Poisson's ratio (v)		
	β_{min}	β_{max}	A	Y_{min}	Y_{max}	A	G_{min}	G_{max}	A	v_{min}	v_{max}	A
FeSc$_2$S$_4$	224 500	224 500	1	0.007639	0.011756	1.54	0.005945	0.032595	5.48	−0.8588	−0.3575	0.42
FeSc$_2$Se$_4$	245 900	245 900	1	0.0082142	0.010612	1.29	0.0083808	0.027174	3.24	−0.8268	−0.5099	0.62

Fig. 4 The electronic band structures for spinel $FeSc_2S_4$ at pressure (a) 0 GPa, (b) 2 GPa and (c) 4 GPa computed with mBJ potential.

up configuration, whereas it reveals metallic nature in the spin down configuration. The electronic band structure, traced along the high symmetry path, shows a moderate degree of band dispersion, particularly in the conduction region.[41] The spin-resolved bands reveal a clear asymmetry between spin-up (red) and spin-down (green) states, particularly near the Fermi level (E_F), confirming the existence of magnetic ordering in the system. This spin splitting arises from the exchange interaction of Fe 3d orbitals, typical for magnetic spinel compounds. The observed band structure suggests localized carrier behavior under ambient pressure. At 2 GPa (Fig. 4(b)), the electronic structure displays significant pressure-induced modifications. The direct band-gap reduces, as both the CBM and VBM are located at the Γ-point, the CBM in the spin-up channel shifts downward, whereas the VBM in the spin-down channel exhibits a slight upward shift.[42] This band-gap narrowing indicates enhanced orbital hybridization and electronic delocalization due to lattice compression. The pressure-driven enhancement in Fe–S–Sc orbital overlap facilitates stronger coupling among Fe-3d, Sc-3d, and S-3p states, which is reflected in the broader conduction band features. At 4 GPa (Fig. 4(c)), the system undergoes further band structure evolution, with the direct band gap decreasing. The CBM at the Γ-position continues to shift toward the E_F, while the VBM at Γ shows negligible movement, maintaining the direct nature of the band gap. Importantly, the spin polarization is preserved across the entire Brillouin zone, confirming the stability of magnetic exchange interactions under high pressure, likely mediated by Fe–S–Fe

superexchange mechanisms intrinsic to the spinel lattice. This pressure-driven tuning of the electronic structure demonstrates the feasibility of modulating spin and charge transport properties, positioning $FeSc_2S_4$ as a promising candidate for spintronic and magneto-functional applications under external pressure stimuli.

3.4. Electronic structure analysis for $FeSc_2Se_4$

Fig. 5(a–c) presents the spin-polarized electronic band structures of the $FeSc_2Se_4$ spinel under pressures of 0 GPa, 2 GPa, and 4 GPa, calculated using the TB-mBJ potential. The energy states are plotted against high symmetry directions of the FCC Brillouin zone. The spin-resolved states provide a detailed depiction of the material's magnetic and electronic response under compression. At 0 GPa, $FeSc_2Se_4$ exhibits a direct semiconducting character because both band edges (VBM and CBM) are positioned at the Γ-point. Upon increasing the pressure to 2 GPa (Fig. 5(b)), the electronic structure displays a reduction in band gap. This band-gap narrowing results from increased orbital overlap due to the contraction of interatomic distances, enhancing the hybridization between Fe-3d, Sc-3d, and Se-4p orbitals. The CBM in spin-up configuration moves downward, and the VBM in the spin-down state shifts upward. This behavior is indicative of increased electronic conductivity and suggests potential for improved thermodynamic performance.[43] At 4 GPa (Fig. 5(c)), a further reduction in band gap was observed. This consistent decrease in the direct band-gap values at 0, 2, and 4 GPa, along with the emergence of spin asymmetry
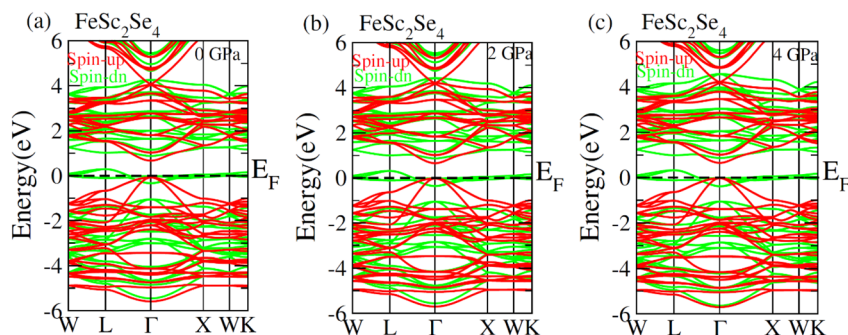

Fig. 5 The electronic band structures for spinel $FeSc_2Se_4$ at pressure (a) 0 GPa, (b) 2 GPa and (c) 4 GPa computed with mBJ potential.

and half-metallicity, highlights the potential of $FeSc_2Se_4$ as a pressure-tunable quantum material for future spin-based and energy-related device architectures.

To get further insight, total and partial density of states (DOS) profiles are presented in Fig. 6 and 7 offer a detailed understanding of the pressure-dependent electronic behavior of spinel compounds $FeSc_2S_4$ and $FeSc_2Se_4$. Fig. 6(a and b) illustrates the total DOS for both materials under hydrostatic pressures of 0, 2, and 4 GPa, resolved into spin-up and down configurations. For $FeSc_2S_4$, a distinct asymmetry between spin channels at 0 GPa indicates a spin-polarized ground state with a significant exchange splitting near the E_F. The E_F is located within the band gap in spin spin-down configuration, while the spin-up channel remains semiconducting. As pressure increases to 2 and 4 GPa, the band edges in both spin states shift, and a progressive reduction in the gap is observed.[44] This narrowing of the band-gap and increased DOS at the Fermi level imply enhanced electronic delocalization and possible pressure-induced modifications in magnetic exchange interactions, likely associated with augmented Fe–S–Fe superexchange coupling due to lattice compression.

In contrast, $FeSc_2Se_4$ displays the weaker exchange splitting and reduced spin polarization as demonstrated in Fig. 6(b). The total DOS at 0 GPa reveals finite states at the E_F in both spin channels, consistent with semi-metallic or weakly metallic behavior. Upon applying pressure, modest changes in the DOS distribution occur, which suggest that $FeSc_2Se_4$ retains a relatively low-spin character, likely due to weaker hybridization between Fe-3d and Se-4p orbitals, and broader band dispersion arising from the larger atomic radius and lower electronegativity of Se, which weakens magnetic exchange pathways.

Fig. 7(a and b) provides partial DOS (PDOS) at 0 GPa, decomposing the total electronic states into orbital contributions from Fe and chalcogen atoms. In $FeSc_2S_4$, the Fe-3d states, split into t_{2g} and e_g orbitals due to octahedral ligand fields, dominate the DOS near the E_F. A pronounced exchange splitting is evident, with the spin-up e_g states located well below E_F and the t_{2g} states lying just above E_F, supporting a high-spin Fe^{2+} configuration. The 3p orbitals of S show strong hybridization with Fe-3d states in the valence region (-6 to 0 eV), reflecting significant p–d covalency that contributes to the magnetic ordering and electronic transport properties. For $FeSc_2Se_4$, the

Fe-3d orbitals appear more delocalized, with reduced exchange splitting and broader band features. The Se-4p states extend across a wider energy range and hybridize less strongly with Fe-3d orbitals, resulting in diminished localization of magnetic moments and weaker spin polarization.[45] The less distinct orbital separation and broader DOS reflect weaker ligand field effects and support the inference of a lower magnetic ordering in $FeSc_2Se_4$.

Overall, the electronic structure analysis reveals that $FeSc_2S_4$ possesses robust spin-polarized features with a pressure-tunable half-metallic character, while $FeSc_2Se_4$ demonstrates a more delocalized, weakly magnetic nature. The application of pressure modifies the electronic landscape in both materials, but the response is more pronounced in the sulfide analogue, where lattice compression enhances orbital overlap and magnetic interactions. These contrasting behaviors underscore the crucial role of chalcogen anions in dictating the balance between electron localization and delocalization, as well as the stability of magnetic order. Such insights are critical for designing spinel-based materials with tailored magnetic and electronic functionalities for advanced applications in spintronics, magnetoelectrics, and energy conversion technologies.

3.5. Magnetic properties

The magnetic behavior of spinel-structured compounds is a critical determinant of their functional viability across a range of spintronic and magneto-electronic applications. In this study, the magnetic properties of $FeSc_2Z_4$ (Z = S, Se) spinels were systematically evaluated by computing both the total and site-resolved magnetic moments using DFT. The quantitative results are summarized in Table 3, which details the total, interstitial, and atomic site-specific magnetic moments expressed in Bohr magnetons (μ_B). For both $FeSc_2S_4$ and $FeSc_2Se_4$, the total magnetic moment of the unit cell was calculated to be $4.000\mu_B$. This net moment primarily arises from the Fe^{2+} ions, which occupy tetrahedral sites in the spinel lattice and contribute substantially to the magnetism through their partially filled 3d orbitals.[46] The localized magnetic moment on the Fe site was found to be $\sim3.36\mu_B$ for $FeSc_2S_4$ and $\sim3.31\mu_B$ for $FeSc_2Se_4$. These values are slightly lower than the ideal high-spin configuration of Fe^{2+} ($4\mu_B$), a deviation that can be attributed to covalent interactions and hybridization effects between
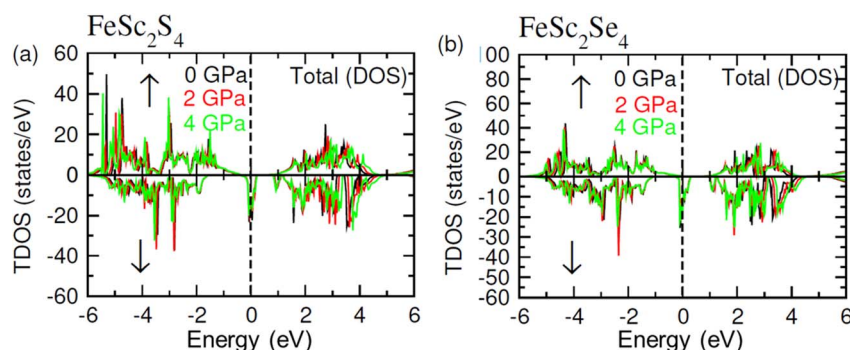

Fig. 6 Total DOS for spinels (a) $FeSc_2S_4$ and (b) $FeSc_2Se_4$ at different pressure in spin–up ($\uparrow$) and spin–down ($\downarrow$), computed with mBJ potential.
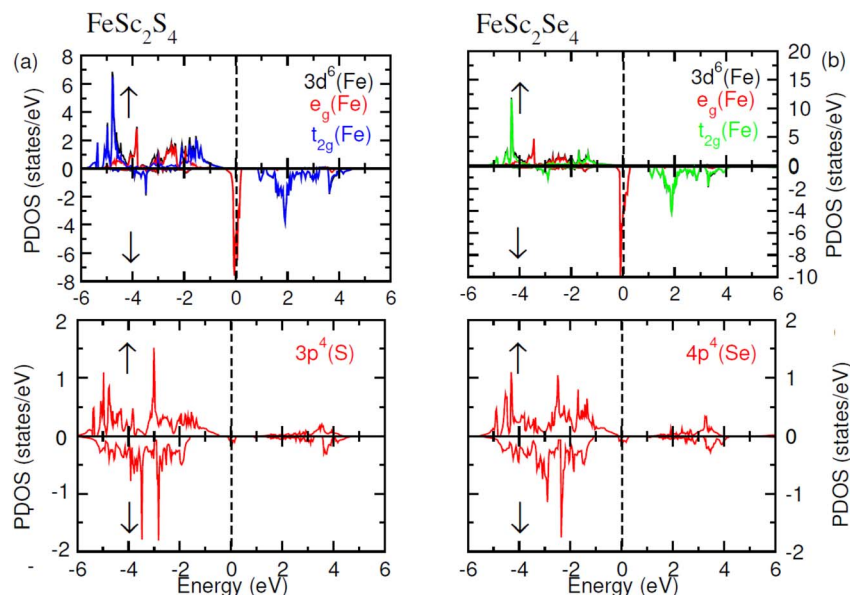
Fig. 7 Partial DOS for spinels (a) $FeSc_2S_4$ and (b) $FeSc_2Se_4$ at 0 GPa in spin-up (↑) and spin-down (↓), computed with mBJ potential.

Table 3 The total, and the local magnetic moments (in Bohr magneton) calculated for $FeSc_2Z_4$ (Z = S, Se)

	Total (μ_B)	Int. (μ_B)	Fe (μ_B)	Sc (μ_B)	Z (μ_B)
$FeSc_2S_4$	4.0000	0.6536	3.3586	0.0647	0.0464
$FeSc_2Se_4$	4.0000	0.6991	3.3079	0.0793	0.0459

Fe-3d orbitals and the surrounding anion (S or Se) p-orbitals. The minor but non-negligible magnetic moments on the nominally non-magnetic sites Sc and the chalcogen Z (S or Se) further support the presence of hybridization-induced magnetic polarization.[47] In both compounds, the Sc atoms contribute magnetic moments of $0.0647\mu_B$ and $0.0793\mu_B$ in $FeSc_2S_4$ and $FeSc_2Se_4$, respectively. These induced moments likely stem from superexchange interactions mediated *via* Fe–Z–Fe pathways and the partial delocalization of spin density into neighboring atoms, especially at the anion sites. Additionally, a small magnetic contribution was noted in the interstitial regions of the unit cell, amounting to ~$0.65\mu_B$ for $FeSc_2S_4$ and ~$0.70\mu B$ for $FeSc_2Se_4$. This observation implies a non-trivial degree of spin delocalization, likely due to the extended character of the Fe-3d states and the larger radial extent of Se-4p orbitals compared to S-3p orbitals, resulting in enhanced orbital overlap and magnetic exchange.[48]

3.6. Thermodynamic properties

To elucidate the temperature and pressure-dependent thermodynamic behavior of $FeSc_2Z_4$ (Z = S, Se) spinels, we employed quasi quasi-harmonic Debye model, as employed in the GIBBS2 computational framework.[49] This methodology allows the accurate estimation of various thermal quantities, including the entropy (S), Debye temperature (θ_D), heat capacity (C_V), and thermal expansion coefficient (α) over a wide temperature range

of 0–1000 K under hydrostatic pressures of 0, 2, and 4 GPa. It should be noted that the thermodynamic results presented up to 600 K are based on the quasi-harmonic Debye model, and while this temperature window is chosen to explore general thermodynamic trends, the physical applicability is constrained by the actual melting and Curie temperatures of $FeSc_2Z_4$. Therefore, results at temperatures beyond these limits should be interpreted as theoretical extrapolations rather than direct experimental predictions. These thermodynamic quantities provide insight into the anharmonic vibrational entropy, mechanical robustness, and phonon behavior of spinels, which are essential for evaluating their applicability in energy-related technologies.[50]

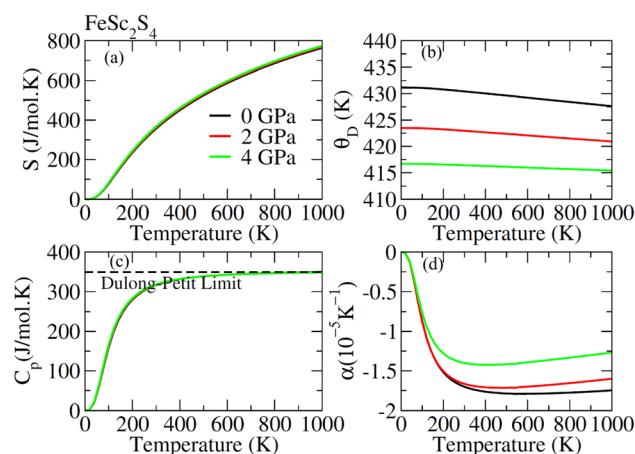Among these parameters, entropy (S) is particularly indicative of the degree of configurational disorder and phonon

Fig. 8 Calculated values of (a) entropy, (b) Debye temperature (c) C_p and (d) coefficient of thermal expansion (α) for spinel $FeSc_2S_4$ at different pressure.

population within a crystal lattice. As shown in Fig. 8 and 9(a), S increases monotonically with temperature, approaching zero at 0 K, consistent with the third law of thermodynamics.[51] The rate of entropy increase is steep at lower temperatures due to rapid phonon excitation, eventually tapering off at higher temperatures as phonon modes become fully populated. Notably, the effect of pressure on S is more pronounced in $FeSc_2Se_4$ at higher temperatures. At 300 K and 0 GPa, the entropy values were found to be 340 for $FeSc_2S_4$ and 405 J mol^{-1} K^{-1} for $FeSc_2Se_4$, as illustrated in Fig. 8 and 9(a). This progressive increase from S to Se reflects the higher atomic mass and increased number of vibrational degrees of freedom in the heavier spinels.[52]

The evolution of entropy with temperature and pressure is intrinsically linked to the behavior of Debye temperature (θ_D), which describes the vibrational spectrum and stiffness of the material. As illustrated in Fig. 8 and 9(b), the Debye temperature (θ_D) remains relatively constant at cryogenic temperatures but exhibits a noticeable linear decline beyond approximately 280 K for $FeSc_2S_4$ and 220 K for $FeSc_2Se_4$. This behavior is attributed to phonon softening and enhanced anharmonic effects at elevated temperatures.[53] In contrast, θ_D decreases nearly linearly with pressure for $FeSc_2S_4$, whereas it increases for $FeSc_2Se_4$, indicating enhanced interatomic interactions and stiffer lattice dynamics under compression in the latter. This pressure-induced hardening of the phonon modes complements the observed suppression of entropy and signifies an ordered, rigid structure at high pressure. At 300 K and 0 GPa, the θ_D values were calculated to be 450 K ($FeSc_2S_4$), and 360 K ($FeSc_2Se_4$), revealing an inverse correlation with atomic mass. This inverse trend further confirms that lighter elements form stronger bonds and possess higher phonon frequencies, which, in turn, influence both entropy and thermal conductivity.

The interplay between S and θ_D also governs the behavior of the heat capacity (C_V), which is primarily governed by phonon excitation. Fig. 8 and 9(c) show that C_V exhibits a characteristic T^3 dependence at low temperatures, consistent with Debye theory, and approaches the classical Dulong–Petit limit at elevated temperatures as all phonon modes are thermally

activated.[54] This transition from quantum to classical regime occurs more prominently below 220 K, after which the heat capacity increases slowly and asymptotically saturates. Importantly, pressure exerts only a marginal influence on C_V, causing a slight decrease due to suppression of lattice vibrations under compression.[55] At 300 K and 0 GPa, the computed C_V values are 305 for $FeSc_2S_4$ and 325 J mol^{-1} K^{-1} for $FeSc_2Se_4$, demonstrating a mass and structure-dependent increase that parallels the trends observed in entropy.[56] In addition, the coefficient of thermal expansion (α) was also computed to assess the volumetric response of these spinels to thermal stimuli under varying pressures. As depicted in Fig. 8 and 9(d), α demonstrates a pronounced sensitivity to both temperature and pressure, with its behavior closely paralleling that of C_V, albeit with a heightened pressure dependence. At lower temperatures, α exhibits a steep increase, indicative of anharmonic lattice vibrations becoming more prominent as thermal energy accumulates. This trend gradually attenuates at elevated temperatures, where α tends to plateau, reaching quasi-saturation a characteristic response of materials approaching their classical Dulong–Petit limit.[57] Quantitatively, at ambient pressure (0 GPa) and 300 K, α was determined to be 6.147×10^{-5} K^{-1} for $FeSc_2S_4$, and 5.0×10^{-5} K^{-1} for $FeSc_2Se_4$. The relatively higher α value in the selenide compound compared to its sulfide counterpart can be attributed to the larger atomic radius and increased polarizability of selenium, which reduces lattice stiffness and enhances vibrational anharmonicity under thermal excitation. This intrinsic softening of the Fe–Se and Sc–Se bonds facilitates a greater volumetric response to temperature. Furthermore, with the application of hydrostatic pressure, a noticeable decline in α is observed for both systems, consistent with the general thermodynamic behavior of condensed matter under compression.[58] This reduction arises from pressure-induced suppression of lattice vibrations and diminished anharmonic interactions, leading to increased rigidity and reduced thermal dilatation.

3.7. Phonon dispersion

In the present communication, the Phonon dispersion analyses were performed using the Phonopy package.[59] For cubic symmetry, the dynamical stability of the investigated spinels requires that the phonon frequencies remain positive at the Γ-point. Our unit-cell-based phonon calculations within the
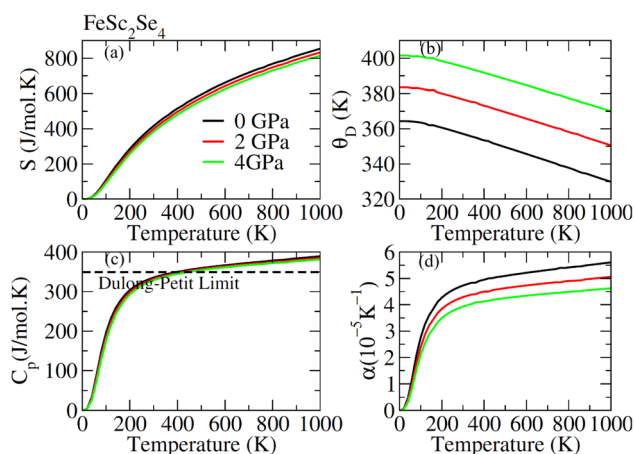

Fig. 9 Calculated values of (a) entropy, (b) Debye temperature (c) C_p and (d) coefficient of thermal expansion (α) for spinel $FeSc_2Se_4$ at different pressure.

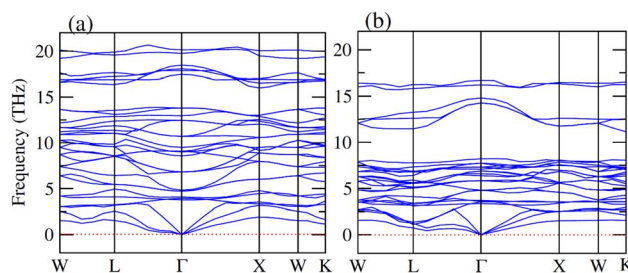Fig. 10 Phonon dispersion curve for spinels (a) $FeSc_2S_4$ and (b) $FeSc_2Se_4$.

Brillouin zone confirmed that $FeSc_2Z_4$ (Z = S, Se) is dynamically stable, as illustrated in Fig. 10(a and b). The primitive cell of each spinel structure contains seven atoms, giving rise to three acoustic branches and eighteen optical vibrational modes, as displayed in Fig. 10(a and b). The absence of gaps between the optical branches indicates a uniform distribution of atomic masses in the lattice. Moreover, phonon spectra obtained from the pre-optimized geometries further verify the dynamical robustness of these compounds, suggesting their suitability for potential spintronic applications.[60]

4. Conclusion

In the current report, the structural, mechanical, electronic, magnetic, and thermodynamic characteristics of $FeSc_2Z_4$ (Z = S, Se) spinels were comprehensively investigated using the density functional theory-based WIEN2k code. The optimized structural parameters were noted as 10.35 Å, and 10.83 Å for $FeSc_2S_4$ and $FeSc_2Se_4$, respectively. The calculated formation enthalpies of −1.67 eV for $FeSc_2S_4$ and −1.13 eV for $FeSc_2Se_4$ confirmed the thermodynamic stability of both compounds, with $FeSc_2S_4$ exhibiting comparatively higher thermodynamic stability. Mechanical property evaluation exhibited the Poisson's ratio of 0.31 ($FeSc_2S_4$) and 0.32 ($FeSc_2Se_4$), along with B_0/G ratio of 2.31 and 2.44. From electronic analysis, both materials exhibited a pressure-induced narrowing of the direct band gaps, retaining semiconducting behavior in the spin-up channel and metallic character in the spin-down channel. Magnetic calculations yielded a total magnetic moment of $4.00\mu_B$ per formula unit for both compounds, primarily contributed by the Fe atoms, confirming the presence of robust ferrimagnetic ordering. Additionally, pressure and temperature-dependent thermodynamic response was evaluated utilizing quasi quasi-harmonic Debye model through the GIBBS2 code. The results demonstrated that entropy and Debye temperature varied systematically with temperature and pressure, providing valuable insights into anharmonic lattice vibrations and thermal stability. The entropy values at 300 K and ambient pressure were calculated to be 340 J mol^{-1} K^{-1} for $FeSc_2S_4$ and 405 J mol^{-1} K^{-1} for $FeSc_2Se_4$, while the corresponding Debye temperatures were 450 K and 360 K, respectively. These trends highlighted the potential of $FeSc_2Z_4$ (Z = S, Se) spinels for next-generation spintronic devices, magneto-optoelectronic systems.

Conflicts of interest

There are no conflicts to declare.

Data availability

All data presented in this paper will be available on demand.

Acknowledgements

References

1 Y. Xie, S. Y. Zhang, Y. Yin, N. Zheng, A. Ali, M. Younis, S. Ruan and Y. J. Zeng, Emerging ferromagnetic materials for electrical spin injection: towards semiconductor spintronics, *npj Spintronics*, 2025, **3**(1), 10.

2 J. A. Incorvia, T. P. Xiao, N. Zogbi, A. Naeemi, C. Adelmann, F. Catthoor, M. Tahoori, F. Casanova, M. Becherer, G. Prenat and S. Couet, Spintronics for achieving system-level energy-efficient logic, *Nat. Rev. Electr. Eng.*, 2024, **1**(11), 700–713.

3 L. Bai, W. Feng, S. Liu, L. Šmejkal, Y. Mokrousov and Y. Yao, Altermagnetism: Exploring new frontiers in magnetism and spintronics, *Adv. Funct. Mater.*, 2024, **34**(49), 2409327.

4 L. Zhang, Y. Liu, M. Wu and G. Gao, Electric-Field-and Stacking-Tuned Antiferromagnetic FeClF Bilayer: The Coexistence of Bipolar Magnetic Semiconductor and Anomalous Valley Hall Effect, *Adv. Funct. Mater.*, 2025, **35**(17), 2417857.

5 J. Han, R. Cheng, L. Liu, H. Ohno and S. Fukami, Coherent antiferromagnetic spintronics, *Nat. Mater.*, 2023, **22**(6), 684–695.

6 F. Trier, P. Noël, J. V. Kim, J. P. Attané, L. Vila and M. Bibes, Oxide spin-orbitronics: spin–charge interconversion and topological spin textures, *Nat. Rev. Mater.*, 2022, 7(4), 258–274.

7 M. Robail, N. A. Noor, M. W. Iqbal, H. Ullah, A. Mahmood, M. A. Naeem and Y. H. Shin, Comprehensive study of ferromagnetic $MgNd_2X_4$ (X= S, Se) spinels for spintronic and solar cells device applications, *Ceram. Int.*, 2022, **48**(2), 2385–2393.

8 A. W. Hooch, S. Lee, H. S. Lee, H. Shin, T. Y. Yoo, W. Ko, J. Shim, G. Na, Y. E. Sung and T. Hyeon, High-valence metal-driven electronic modulation for boosting oxygen evolution reaction in high-entropy spinel oxide, *Adv. Funct. Mater.*, 2024, **34**(1), 2309438.

9 L. Zhang, Y. Liu, Z. Xu and G. Gao, Electronic phase transition, perpendicular magnetic anisotropy and high Curie temperature in Janus FeClF, *2D Mater.*, 2023, **10**(4), 045005.

10 M. A. Yasir, N. A. Noor, M. A. Khan, S. Niaz, S. Mumtaz, I. M. Moussa and H. Ullah, Spin-polarized analysis of ferromagnetism, optoelectronic and transport characteristics of $HgGd_2(S/Se)_4$ spinels: DFT-calculations, *Mater. Today Commun.*, 2025, **43**, 111636.

11 A. A. Mousa, S. M. Al Azar, S. S. Essaoud, K. Berarma, A. Awad, N. T. Mahmoud, E. K. Jaradat and M. S. Abu-Jafar, Structural, Elastic, Electronic, Magnetic, and Thermoelectric Characteristics of $MgEu_2X_4$ (X= S, Se) Spinel Compounds: Ab-Initio Calculations, *Phys. Status Solidi B*, 2022, **259**(10), 2200191.

12 I. C. Abiodun, M. E. Edem and O. E. Agbor, Investigation of the Structural and electronic properties of Ternary AB_2X_4 based material via Density Functional Theory (DFT) for

Optoelectronic Applications, *Commun. Phys. Sci.*, 2024, **12**(1), 1.

13 A. Bouhemadou, D. Allali, K. Boudiaf, B. Al Qarni, S. Bin-Omran, R. Khenata and Y. Al-Douri, Electronic, optical, elastic, thermoelectric and thermodynamic properties of the spinel oxides $ZnRh_2O_4$ and $CdRh_2O_4$, *J. Alloys Compd.*, 2019, **774**, 299–314.

14 B. O. Alsobhi and A. Almeshal, Structural, elastic, thermodynamic, electronic, magnetic, thermoelectric and optical investigation of chromate spinels TCr_2O_4 [T= V^{2+}, Mn^{2+}, Fe^{2+}] for optoelectronic applications, *Mater. Chem. Phys.*, 2023, **294**, 127041.

15 M. A. Haq, M. Javed, R. Mumtaz, H. Ullah, A. ur Rehman, S. M. Wabaidur, Z. Ahmad and M. Zafar, Mechanical and thermal response of XFe_2O_4 (X= Zn, Ag and Co) spinel ferrites via IR-spectroscopy and first-principles calculations, *Phys. Scr.*, 2024, **99**(4), 045935.

16 F. Ak, E. G. Özdemir and H. A. Aliabad, Semiconducting character analysis of RhY_2O_4 oxide spinel via GGA, GGA+ mBJ, and GGA+ U approximations, *Indian J. Phys.*, 2025, **9**, 1.

17 E. G. Özdemir and F. I. Balmumcu, Magnetic, pressure-dependent elastic, and band gap calculations of VCo_2O_4 oxide spinel via GGA, GGA+ mBJ, and GGA+ U, *Phys. B*, 2024, **674**, 415544.

18 E. G. Özdemir and S. Doğruer, Electronic, magnetic, and pressure-induced elastic investigaments of MnY_2O_4 oxide spinel, *Eur. Phys. J. Plus*, 2023, **138**(1), 23.

19 E. G. Özdemir, Z. Merdan and H. R. Aliabad, Effects of applied different potentials on electronic and Half-Metallic characteristics and investigated Pressure-Dependent elastic and thermodynamic properties of VRu2Br4 spinel, *J. Magn. Magn. Mater.*, 2024, **590**, 171671.

20 E. G. Özdemir and S. Doğruer, The structural, magnetic, and pressure-induced elastic predictions of $ZrPd_2O_4$ oxide spinel via GGA, GGA+ mBJ, and GGA+ U approximations, *J. Magn. Magn. Mater.*, 2023, **568**, 170417.

21 S. A. Raza, G. M. Mustafa, M. A. Ameer, N. A. Noor, Z. Farooq, S. Mumtaz and I. M. Moussa, Investigation of $MnSc_2X_4$ (X= S, Se) spinels to unveil their potential for optoelectronic and thermoelectric applications, *RSC Adv.*, 2025, **15**(13), 9662–9675.

22 Y. G. Kartal, W. A. Ahmed, E. G. Özdemir, S. Doğruer, F. I. Balmumcu and Z. Merdan, An alternative material obtained for spintronic applications using first-principles approximations: TiV_2Se_4 spinel, *Theor. Chem. Acc.*, 2025, **144**(2), 16.

23 A. Qadoos, M. Rashid, N. D. Alkhaldi, N. M. Alresheedi, I. Boukhris, Q. Mahmood and M. N. Nasir, Electronic, magnetic, optical, and thermoelectric properties of rare earth-based $CaCe_2(S/Se)_4$ spinels for spintronic and energy harvesting applications, *J. Rare Earths*, 2025, DOI: 10.1016/j.jre.2025.02.017.

24 N. A. Kattan, S. A. Rouf, H. D. Alkhaldi, M. Hassan, S. Al-Qaisi, A. I. Aljameel, H. Albalawi, I. Boukhris, Q. Mahmood and U. Mumtaz, Study of Half Metallic Ferromagnetism and Thermoelectric Properties of the Spinels $MgCo_2(S/Se)_4$

for Spintronic and Energy Harvesting, *J. Inorg. Organomet. Polym. Mater.*, 2025, **35**(2), 724–737.

25 I. Jamaï, M. Ziati, N. Bekkioui and H. Ez-Zahraouy, Structural, electronic, optical, thermoelectric, and thermodynamic properties of XIn_2M_4 (X= Cd, Zn; M= S, Se, Te) spinels for solar cell and thermoelectric devices: first-principles study, *Phys. Scr.*, 2024, **99**(10), 105936.

26 P. Blaha, K. Schwarz, G. K. Madsen, D. Kvasnicka and J. Luitz, *Wien2k: An augmented plane wave+ local orbitals program for calculating crystal properties*, 2001, vol. 60.

27 M. Petersen, F. Wagner, L. Hufnagel, M. Scheffler, P. Blaha and K. Schwarz, Improving the efficiency of FP-LAPW calculations, *Comput. Phys. Commun.*, 2000, **126**(3), 294–309.

28 D. Koller, F. Tran and P. Blaha, Improving the modified Becke-Johnson exchange potential, *Phys. Rev. B: Condens. Matter Mater. Phys.*, 2012, **85**(15), 155109.

29 A. Otero-de-la-Roza and V. Luana, Gibbs2: A new version of the quasi-harmonic model code. I. Robust treatment of the static data, *Comput. Phys. Commun.*, 2011, **182**(8), 1708–1720.

30 N. A. Noor, M. Hassan, M. Rashid, S. M. Alay-e-Abbas and A. Laref, Systematic study of elastic, electronic, optical and thermoelectric properties of cubic $BiBO_3$ and $BiAlO_3$ compounds at different pressure by using ab-initio calculations, *Mater. Res. Bull.*, 2018, **97**, 436–443.

31 Q. Mahmood, N. A. Noor, M. Jadan, J. S. Addasi, A. Mahmood and S. M. Ramay, First-principle investigation of ferromagnetism and thermoelectric characteristics of $MgCr_2X_4$ (X= S, Se) spinels, *J. Solid State Chem.*, 2020, **285**, 121261.

32 S. A. Raza, G. M. Mustafa, M. A. Ameer, N. A. Noor, Z. Farooq, S. Mumtaz and I. M. Moussa, Investigation of $MnSc_2X_4$ (X= S, Se) spinels to unveil their potential for optoelectronic and thermoelectric applications, *RSC Adv.*, 2025, **15**(13), 9662–9675.

33 J. R. Morey, K. W. Plumb, C. M. Pasco, B. A. Trump, T. M. McQueen and S. M. Koohpayeh, Growth and characterization of iron scandium sulfide ($FeSc_2S_4$), *J. Cryst. Growth*, 2016, **454**, 128–133.

34 R. D. Shannon, Revised effective ionic radii and systematic studies of interatomic distances in halides and chalcogenides, *Acta Crystallogr., Sect. A: Found. Crystallogr.*, 1976, **32**(5), 751–767.

35 L. Zhang, Y. Zhao, Y. Liu and G. Gao, High spin polarization, large perpendicular magnetic anisotropy and room-temperature ferromagnetism by biaxial strain and carrier doping in Janus MnSeTe and MnSTe, *Nanoscale*, 2023, **15**(46), 18910–18919.

36 M. A. Ali and S. H. Naqib, Recently synthesized $(Ti_{1-x}Mo_x)_2AlC$ ($0\leq$ x$\leq$ 0.20) solid solutions: deciphering the structural, electronic, mechanical and thermodynamic properties via ab initio simulations, *RSC Adv.*, 2020, **10**(52), 31535–31546.

37 M. W. Qureshi, M. A. Ali and X. Ma, Screen the thermomechanical and optical properties of the new ductile 314 MAX phase boride Zr_3CdB_4: A DFT insight, *J. Alloys Compd.*, 2021, **877**, 160248.

38 M. A. Ali, M. M. Hossain, M. M. Uddin, M. A. Hossain, A. K. Islam and S. H. Naqib, Physical properties of new MAX phase borides M_2SB (M= Zr, Hf and Nb) in comparison with conventional MAX phase carbides M_2SC (M= Zr, Hf and Nb): Comprehensive insights, *J. Mater. Res. Technol.*, 2021, **11**, 1000–1018.

39 Q. Fan, W. Zhang, S. Yun, J. Xu and Y. Song, III-nitride polymorphs: XN (X= Al, Ga, In) in the Pnma phase, *Chem.–Eur. J.*, 2018, **24**(65), 17280–17287.

40 W. Zhang, C. Chai, Q. Fan, Y. Song and Y. Yang, Six novel carbon and silicon allotropes with their potential application in photovoltaic field, *J. Phys.: Condens. Matter*, 2020, **32**(35), 355701.

41 V. S. Zhandun, The magnetic, electronic, optical, and structural properties of the AB_2O_4 (A= Mn, Fe, co; B= Al, Ga, In) spinels: Ab initio study, *J. Magn. Magn. Mater.*, 2021, **533**, 168015.

42 S. Maqsood, M. A. Javed, S. Mumtaz and M. K. Al-Sadoon, Computational study of Cd-based chalcogenide spinels $CdSm_2(S/Se)_4$ for spintronic applications, *Chalcogenide Lett.*, 2024, **21**(6), 449–458.

43 Q. Mahmood, G. Nazir, J. Alzahrani, N. A. Kattan, S. Al-Qaisi, H. Albalawi, A. Mera, G. A. Mersal, M. M. Ibrahim and M. A. Amin, Room temperature ferromagnetism and thermoelectric behavior of calcium based spinel chalcogenides CaZ_2S_4 (Z= Ti, V, Cr, Fe) for spintronic applications, *J. Phys. Chem. Solids*, 2022, **167**, 110742.

44 M. Al-Qhtani, G. M. Mustafa, N. Mazhar, S. Bouzgarrou, Q. Mahmood, A. Mera, Z. I. Zaki, N. Y. Mostafa, S. H. Alotaibi and M. A. Amin, Half metallic ferromagnetism and transport properties of zinc chalcogenides ZnX_2Se_4 (X= Ti, V, Cr) for spintronic applications, *Materials*, 2021, **15**(1), 55.

45 T. M. Al-Daraghmeh, O. Zayed, G. M. Mustafa, T. Zelai, B. Younas, H. Albalawi, S. Bouzgarrou, O. Hakami, Q. Mahmood and K. I. Hussein, Rare earth based $MgPm_2X_4$ (X= S, Se) spinel chalcogenides for spintronic and thermoelectric applications, *J. Rare Earths*, 2024, **42**(8), 1577–1585.

46 H. Raebiger, A. Ayuela and R. M. Nieminen, Intrinsic hole localization mechanism in magnetic semiconductors, *J. Phys.: Condens. Matter*, 2004, **16**(41), L457.

47 Y. Saeed, S. Nazir, A. Shaukat and A. H. Reshak, Ab-initio calculations of Co-based diluted magnetic semiconductors $Cd_{1-x}Co_xX$ (X= S, Se, Te), *J. Magn. Magn. Mater.*, 2010, **322**(20), 3214–3222.

48 I. Elahi, S. M. Alay-e-Abbas, S. Nazir, A. Shaukat and M. N. Tahir, Evaluation of thermodynamics and p-type ferromagnetism of C, Si and Ge doped ZnX (X= S, Se and Te) semiconductors, *J. Magn. Magn. Mater.*, 2019, **477**, 249–257.

49 A. Hosen, D. Dahliah, N. F. Mohammad, A. A. Mousa and M. S. Abu-Jafar, A computational study on the comparative analysis of tetragonal complex metal hydride Q_2FeH_5 (Q= Mg, Ca, Sr) for hydrogen storage applications, *Int. J. Hydrogen Energy*, 2025, **102**, 348–359.

50 B. Gurunani, S. Ghosh and D. C. Gupta, Comprehensive investigation of half Heusler alloy: Unveiling structural, electronic, magnetic, mechanical, thermodynamic, and transport properties, *Intermetallics*, 2024, **170**, 108311.

51 V. Shukla, A. Bhatnagar, S. K. Verma, A. P. Pandey, A. K. Vishwakarma, P. Srivastava, T. P. Yadav and O. N. Srivastava, Simultaneous improvement of kinetics and thermodynamics based on SrF_2 and $SrF_2@Gr$ additives on hydrogen sorption in MgH_2, *Mater. Adv.*, 2021, **2**(13), 4277–4290.

52 B. Gurunani and D. C. Gupta, First-principles investigation of thermoelectric performance in KMnZ (Z= Sn, Pb) half-Heusler alloys, *RSC Adv.*, 2025, **15**(7), 4874–4891.

53 G. P. Johari, Entropy, enthalpy and volume of perfect crystals at limiting high pressure and the third law of thermodynamics, *Thermochim. Acta*, 2021, **698**, 178891.

54 P. L. Dulong and A. T. Petit, *Recherches sur quelques points importans de la theorie de la chaleur*, 1819.

55 D. Marx and J. Hutter, *Ab Initio Molecular Dynamics: Basic Theory and Advanced Methods*, Cambridge University Press, 2009.

56 G. M. Mustafa, B. Younas, H. D. Alkhaldi, A. Mera, A. K. Alqorashi, J. Hakami, S. A. Mahmoud, I. Boukhris and Q. Mahmood, First principle study of physical aspects and hydrogen storage capacity of magnesium-based double perovskite hydrides Mg_2XH_6 (X= Cr, Mn), *Int. J. Hydrogen Energy*, 2024, **95**, 300–308.

57 E. I. Andritsos, E. Zarkadoula, A. E. Phillips, M. T. Dove, C. J. Walker, V. V. Brazhkin and K. Trachenko, The heat capacity of matter beyond the Dulong–Petit value, *J. Phys.: Condens. Matter*, 2013, **25**(23), 235401.

58 T. Saadi, H. Baaziz, T. Ghellab, H. Latelli, A. Telfah and Z. Charifi, Electronic structure, mechanical and optical properties of hydrogen storage alkaline amides XNH_2 (X= Li, Na) compounds, *Int. J. Hydrogen Energy*, 2025, **102**, 1480–1496.

59 W. Yi, G. Tang, X. Chen, B. Yang and X. Liu, qvasp: A flexible toolkit for VASP users in materials simulations, *Comput. Phys. Commun.*, 2020, **257**, 107535.

60 H. A. Alburaih, N. A. Noor, M. Rashid, S. Nazir and A. Laref, Tuning of electronic bandgap and electronic transport properties of double perovksites A_2NaScI_6 (A= Rb, Cs) for energy device applications, *Phys. Scr.*, 2023, **98**(2), 025701.